ARTICLE IN PRESS

Journal of Industrial and Engineering Chemistry xxx (xxxx) xxx



Contents lists available at ScienceDirect

Journal of Industrial and Engineering Chemistry

journal homepage: www.elsevier.com/locate/jiec



Full length article

Gadolinium doped ZnS particles as electrode material for supercapacitor application †

Ion Nesterovschi ^{a,b}, Ameen Uddin Ammar ^a, Alexander Bunge ^a, Adriana Popa ^a, Maria Stefan ^a, Sergiu Macavei ^a, Iolanda Ganea ^a, Marin Senila ^c, Emre Erdem ^{a,d}, Arpad Mihai Rostas ^a, Dana Toloman ^a, *

- a National Institute for Research and Development of Isotopic and Molecular Technologies, Donat 67-103, Cluj-Napoca, 400293, Romania
- ^b Doctoral School of Physics, Babes-Bolyai University, Cluj-Napoca, 400084, Romania
- c Res Inst Analyt Instrumentat, INCDO INOE 2000, Donat 67, Cluj-Napocal, 400293, Romania
- ^d Faculty of Engineering and Natural Sciences, Sabanci University, Tuzla, Istanbul, 34956, Turkey

ARTICLE INFO

Keywords: ZnS Gadolinium Supercapacitors Electron paramagnetic resonance Raman

ABSTRACT

Supercapacitors (SC) have gained prominence among many advanced technologies because of their superior power density, fast charge/discharge capabilities, extended cycle lifespan, and remarkable operational stability. Recent advancements in ZnS nanostructures underscore their potential for high-performance SCs, especially when their morphology and surface characteristics are carefully engineered. Incorporating dopants into ZnS has proven effective in further enhancing its electrochemical performance. Adding dopants into the ZnS lattice results in defects, such as zinc and sulfur vacancies and interstitial atoms. In this study, ZnS doped with varying concentrations of Gd ions serves as an electrode material in supercapacitor devices. The influence of the induced defect states and Gd-ions concentration, characterized by photoluminescence, Raman, and electron paramagnetic resonance spectroscopy, on the electrochemical properties was demonstrated through cyclic voltammetry, potentiostatic electrochemical impedance spectroscopy, and galvanostatic cycling with potential limitation. The findings indicate that ZnS doped with a nominal concentration of 0.5% Gd has the highest specific capacitance value, achieving a maximum of 114.7 F/g at 2 mV/s, and demonstrates excellent cyclic stability, retaining about 98% of its capacity after 2000 cycles. It also showcases impressive performance in terms of energy and power density, with values reaching up to 15.93 Wh/kg and 1146 W/kg, respectively. These findings underscore the potential of Gd-doped ZnS as high-efficiency electrodes in supercapacitors, playing a crucial role in advancing sustainable and efficient energy storage solutions that effectively balance energy and power density.

Introduction

Due to increased global energy needs and a further decline in fossil fuel reserves, developing high-performance energy storage systems to enable a partial transition toward renewable energy sources has become urgent [1,2]. Renewable energy, often termed clean energy, is primarily derived from natural resources. Despite its environmental benefits, renewable energy is not always the most effective alternative to fossil fuels in resolving the current global energy crisis and pollution challenges [3]. Therefore, there is a critical need for electrochemical energy storage technologies that are efficient, reliable, and sustainable to meet future energy demands. Among several developed technologies so far, supercapacitors (SC) have come to the front line owing to

their high-power density, high charge/discharge rates, long cyclic life, and excellent operational stability [4,5]. These attributes render SCs highly attractive for critical applications, including electric vehicles, portable electronics, and renewable energy systems [6]. Nevertheless, the broader utilization of SCs is still limited due to their naturally lower energy density when compared to traditional batteries, which have their limitation regarding lower power density and cycle life [7–9]. Thus, a primary research emphasis is boosting energy density by improving specific capacitance and operating voltage [10]. Supercapacitors (SCs) can be classified into two main types based on their charge storage mechanisms: electric double-layer capacitors (EDLCs) and pseudocapacitors [11,12]. EDLCs store energy through

E-mail address: dana.toloman@itim-cj.ro (D. Toloman).

https://doi.org/10.1016/j.jiec.2025.09.014

Received 2 July 2025; Received in revised form 28 August 2025; Accepted 8 September 2025 Available online 19 September 2025

1226-086X/© 2025 The Authors. Published by Elsevier B.V. on behalf of The Korean Society of Industrial and Engineering Chemistry. This is an open access article under the CC BY-NC-ND license (http://creativecommons.org/licenses/by-nc-nd/4.0/).

^{*} Corresponding author.

electrostatic charge accumulation at the electrode–electrolyte interface and typically utilize carbon-based materials—such as activated carbon and carbon nanotubes—as electroactive layers. These materials offer advantages like rapid charge–discharge cycles and excellent long-term stability [13]. In contrast, pseudocapacitors rely on fast and reversible Faradaic redox reactions occurring between the electrode and the electrolyte, enabling high energy storage efficiency [14,15].

The performance of supercapacitors, especially their specific capacitance, is largely influenced by the choice of electrode material [16]. An optimal electrode material should possess a large surface area, high porosity, numerous electrochemically active sites, high electrical conductivity, and a defect structure that supports effective charge storage. [17,18]. Nanostructured semiconductors have gained prominence due to their tunable electronic properties and potential for synergistic enhancements when doped with other elements [19,20]. Among these materials, ZnS has attracted significant interest due to its excellent chemical stability as a II–VI semiconductor with a bandgap of 3.5–3.8 eV [21] and some superiorities of nanoparticles, including low diffusion resistance and fast electron transportation [22]. On the other hand, its intrinsic low conductivity severely hinders ZnS's charge storage capacity [23].

Recent advances in ZnS nanostructures underscore their potential for high-performance SCs, particularly when their morphology and surface characteristics are carefully engineered [24]. Hydrothermal and sol–gel synthesis methods have been utilized to fabricate ZnS nanostructures with enhanced surface area and electroactive sites, significantly boosting their electrochemical properties [25]. ZnS nanoparticles synthesized via hydrothermal methods achieved a specific capacitance of 824 F/g at 1 A/g, maintaining an impressive 93.1% retention after 10,000 charge–discharge cycles [24]. Maintaining high performance at large current densities further highlights ZnS's potential in supercapacitor applications.

Incorporating dopants into ZnS has shown promise for further enhancing its electrochemical performance. The introduction of dopants into the ZnS lattice induces the formation of defects, such as zinc (V_{7n}) and sulfur (V_S) vacancies and interstitial atoms (Zn_i/S_i) [26]. These vacancies introduce localized states within the bandgap, enhancing both conductivity and charge transport. Additionally, dopants can influence crystallite size, strain, and surface chemistry, all of which impact key electrochemical properties such as capacitance, charge storage efficiency, and cycling stability [26-28]. The beneficial effects of doping on electrochemical performance are evident in experimental studies. For example, Ni-doped ZnS microspheres synthesized via hydrothermal methods demonstrated an improved specific capacitance of 104.2 F/g at 5 A/g, compared to 67.75 F/g for undoped ZnS [29]. Similarly, Co-doped ZnS synthesized by co-precipitation showed a substantial increase in specific capacitance from 460.7 F/g for pure ZnS to 947.8 F/g for 5% Co-doped ZnS at a scan rate of 10 mV/s, attributed to the increased electrochemical active sites and enhanced kinetics of redox reactions [30].

Recent studies on Mn-doped ZnS further highlight the role of morphology in enhancing supercapacitor performance. Various nanostructures, such as nanosheets, nanoflakes, and nanoneedles, were synthesized by controlling reaction temperatures. Among these, Mn-doped ZnS nanosheets exhibited the highest specific capacitance of 1905 F/g at 1 A/g and retained 93.1% of their capacity after 10,000 cycles [27]. An asymmetric supercapacitor (ASC) device using Mn-doped ZnS nanosheets and activated carbon achieved an energy density of 43.3 Wh/kg and a power density of 6.8 kW/kg, retaining 93.3% of its capacitance after 8000 cycles, demonstrating the material's excellent stability and practical potential [27]. Additional studies demonstrate the potential of hybrid ZnS materials. Fe-doped ZnS microspheres supported on Ni foam delivered a specific capacitance of 700 F/g at a current density of 0.5 A/g. Meanwhile, hybrid supercapacitor systems incorporating these materials achieved a high energy density of 11 Wh/kg and a power of 591.2 W/kg [31].

The rare-earth doping of ZnS can also introduce localized electronic states within its band structure, enhancing electronic conductivity and charge transfer kinetics. Gadolinium (Gd), with its stable +3 oxidation state, significantly increases the density of electroactive sites, facilitating faster ion transport and enhancing rate capability and cycling stability [32–34].

In this study, ZnS samples doped with different Gd ion concentrations were prepared by a precipitation method for application as electrode materials in supercapacitor devices. A low nominal Gd doping level was chosen that would not affect the crystalline structure of the ZnS but only tune its defects to improve ZnS electrochemical properties. Besides, it is expected that localized states induced by Gd ions to facilitate ion transport and charge transfer. The influence of the induced defect states, characterized by photoluminescence, Raman, and electron paramagnetic resonance spectroscopy, on the electrochemical properties was demonstrated through cyclic voltammetry, potentiostatic electrochemical impedance spectroscopy, galvanostatic cycling with potential limitation, and voltage holding tests. The obtained results emphasize the potential of Gd-doped ZnS particles as high-performance electrodes for supercapacitors, contributing to developing sustainable, efficient energy storage systems capable of bridging the gap between energy and power density.

Materials and methods

Materials

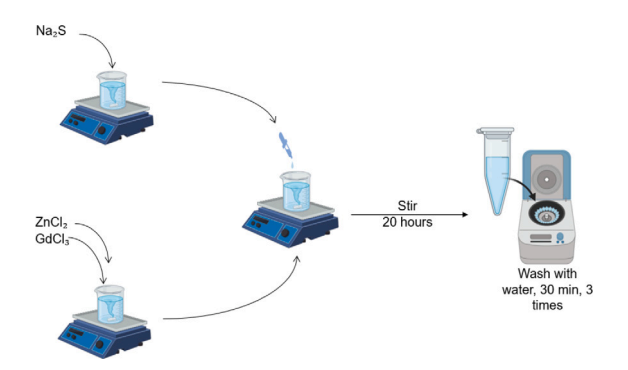
The synthesis procedure employed the following reagents and solvents: Zinc chloride (ZnCl $_2$, 98%, anhydrous) was obtained from Acros, sodium sulfide hydrate (Na $_2$ S · H $_2$ O, p.a., $x\sim7$ -9) from Merck, gadolinium chloride (GdCl $_3$ · 6 H $_2$ O) from Sigma-Aldrich, and KOH from Alfa Aesar for synthesis. Doubly distilled water was used throughout the syntheses.

Synthesis procedure

Both undoped and Gd-doped zinc sulfide samples were prepared using a straightforward precipitation reaction method (see Scheme 1), where an aqueous solution/suspension of zinc chloride (1.022 g, 7.5 mmol) and an aqueous solution of sodium sulfide (0.802 g, 7.5 mmol) were prepared. Additionally, gadolinium chloride (82.4 mg) was dissolved in water (2.942 mL). After adding the respective amounts of gadolinium chloride to the zinc chloride solution, the sodium sulfide solution was added, and the mixture was stirred at room temperature for 20 h. A white powder was obtained after centrifuging, washing with water (3 times), and drying overnight at 60 °C. The obtained samples were denoted as ZnS, ZnS:Gd0.1, ZnS:Gd0.3, ZnS:Gd0.5, ZnS:Gd0.7, and ZnS:Gd1.0 according to the molar percentage of Gd used in the synthesis. The amount of gadolinium chloride solution added was as follows: ZnS: 0 μ L (0 μ mol); ZnS:Gd0.1: 100 μ L (7.5 μ mol); ZnS:Gd0.3: 300 μL (22.5 μ mol); ZnS:Gd0.5: 500 μL (37.5 μ mol); ZnS:Gd0.7: 700 μL (52.5 μ mol); ZnS:Gd1.0: 1000 μ L (75 μ mol).

Characterization methods

The elemental composition of the samples was evaluated using an inductively coupled plasma-optical emission spectrometer, PlasmaQuant 9100 Elite High Resolution ICP-OES. Before analysis, the samples were exposed to microwave-assisted acid digestion in a Berghof Speedwave Entry microwave equipped with 10 high-pressure TFM™-PTFE-quartz vessels. The nanoparticle size and morphology were analyzed using scanning transmission electron microscopy (STEM) with a Hitachi HD2700 microscope equipped with a cold field emission gun, Dual energy dispersive spectroscopy EDS System (X-Max N100TLE Silicon Drift Detector from Oxford Instruments. For the analysis, a suspension of the samples was sonicated with a UP100H ultrasound finger

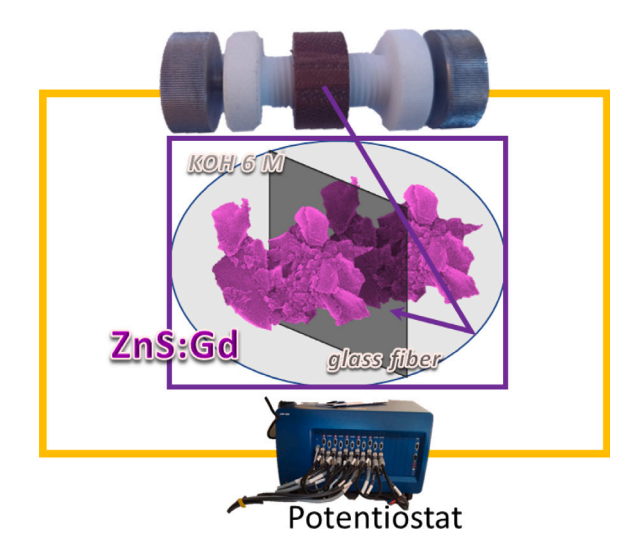


Scheme 1. Schematic representation of the synthesis procedure used to synthesize the undoped and Gd-doped ZnS samples.

and applied via the droplet method onto a 400-mesh copper grid coated with a thin carbon film. The nominal operating tension was 200 kV. A BelSorp MaxX equipment (Microtrac BEL Corporation, Japan) was used to record the N2 sorption isotherms. Pretreatment of samples consisted of degassing under vacuum at 100 °C for 4 h. The standard BET method was used to calculate the specific surface area (p/p_0) range of 0.02-0.25), and total pore volume was estimated at $p/p_0 = 0.95$. X-ray diffraction (XRD) measurements were performed using a Rigaku-SmartLab X-ray Diffractometer with Cu-K radiation at 45 kV, 200 mA. The diffraction patterns were recorded in the range 10–90° with steps of 0.02°. The processing was performed using the Integrated X-ray powder diffraction (PDXL2) software. Fourier transform infrared (FTIR) $\,$ spectra were recorded using a JASCO FTIR 4600 A spectrophotometer with an ATR-PRO-ONE accessory. They underwent CO2, H2O, ATR, and baseline corrections, followed by normalization to enhance the clarity of the bands. The defect structure and the presence of paramagnetic Gd ions were investigated by photoluminescence (PL), Raman, and electron paramagnetic resonance (EPR) spectroscopy. Photoluminescence spectra were recorded using an FS5 spectrofluorometer (Edinburgh Instruments) featuring a 150 W continuous-wave ozone-free Xenon arc lamp, Czerny-Turner monochromators with plane gratings, and a PMT-900 emission detector. Raman spectra were collected using a Renishaw InVia Raman system paired with a Leica microscope. A 785 nm nearinfrared diode laser provided excitation at 130 mW output power. Measurements covered a wavenumber range of 100 to 1250 cm⁻¹ with a spectral resolution of 1 cm⁻¹. EPR spectroscopy measurements were performed on a Bruker E500 ELEXSYS spectrometer at Q-band (33.9 GHz).

Electrochemical properties measurements

Symmetric all-in-one supercapacitor devices were assembled using undoped and Gd-doped ZnS in a 6 M KOH electrolyte, with a glass fiber separator used between the electrodes as depicted in Scheme 2, which represents a circular-shaped stainless-steel bolt on both sides of the device, serving as a current collector. The areal mass loading of the electrodes on this device is approximately 2.65 mg/cm² over an area of 1.13 cm², with a total mass of 3 mg per electrode. Electrode thickness was not specifically measured, as the focus was on maintaining consistent mass loading and electrolyte volume (3 mg of active material with 200 μL of 6 M KOH). A BioLogic VMP 300 electrochemical workstation tested the electrochemical performance of the electrode materials using a two-electrode system. The techniques included cyclic voltammetry (CV), potentiostatic electrochemical impedance spectroscopy (PEIS), and galvanostatic cycling with potential limitation (GCPL). CV measurements were performed within a voltage window of 0 to 1 V, with scan rates varying from 2 to 200 mV/s. PEIS measurements were performed with an AC signal amplitude of 10 mV over a frequency range from 10 mHz to 1 MHz. GCPL tests were conducted at a current density of 0.8 A/g, and the energy and power densities were determined using CV and GCPL data from the best-performing scan rate.



Scheme 2. Schematic representation of the symmetric supercapacitor devices used to assess the electrochemical properties of the undoped and Gd-doped ZnS materials.

Results and discussion

To determine the actual concentrations of Gd in the samples, ICP-OES was used to determine the ratio of Gd/Zn and compare it with the nominal concentration ratio (Table T1*). It can be seen that the actual concentration of Gd found by ICP-OES is lower than the nominal one. This is surprising at first; however, the actual doping percentage increases approximately proportional to the increase in nominal Gd concentration. It is a commonly observed phenomenon that the exact amount of rare earth dopant, and even other dopants such as manganese, is much lower than the nominal one [35–37]. The fact that the ionic radii and charges of the respective cations are too different is the most likely cause for the poor incorporation of gadolinium in the ZnS phase.

The morphology of the samples was determined through STEM measurements; a representative image is shown in Fig. 1(a). All samples exhibit a similar morphology; the STEM image indicates that the material consists of small particles aggregated into larger layered structures with sharp edges. These sharp edges are likely a result of grinding and sonication before measurement. The samples demonstrate that the particles do not disperse well in an aqueous solution, as expected, since no surfactant stabilizes them in dispersion. EDS analysis was used to verify the presence of Gd dopant ions in the ZnS:Gd1.0 sample, as shown in Fig. 1(b); the dopant is uniformly distributed throughout the ZnS particles. More detailed elemental characterization was not carried out because the Gd concentration is very low (< 1%).

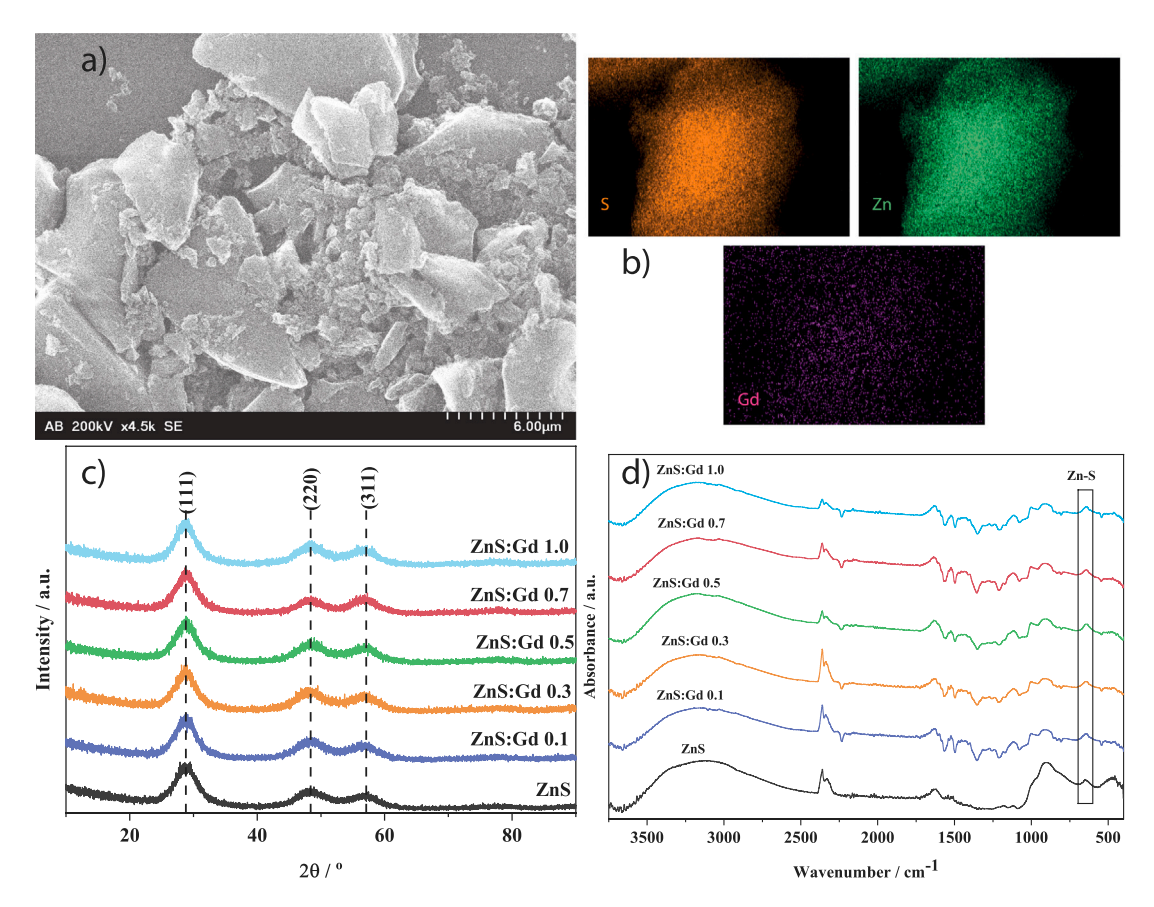


Fig. 1. Representative STEM image (a) of the Gd-doped ZnS samples alongside the EDS (b) elemental mapping of the ZnS:Gd1.0 sample. Diffractograms (c) indexed with the crystallographic planes of the sphalerite structure (cubic F-43 m space group) and FT-IR spectra (d) for all undoped and Gd-doped ZnS samples.

Table 1Results of the Gaussian deconvolution of all undoped and Gd-doped ZnS PL spectra, showing the relative area of each emission band.

Band/nm	Center	ZnS A_x/A_{tot}	ZnS:Gd0.1 × 100/%	ZnS:Gd0.3	ZnS:Gd0.5	ZnS:Gd0.7	ZnS:Gd1.0
410	S_i	9.89	13.95	14.01	12.43	14.03	13.2
433	Zn_i	22.05	31.05	29.43	26.22	29.70	29.33
458	V_s	33	28.66	30.31	32.62	30.18	30.53
503	V_{Zn}	35.05	26.34	26.26	28.73	26.08	26.94

Table 2
Undoped and Gd-doped ZnS Raman spectra peak position and intensities obtained after the Gaussian deconvolution fit.

Sample	Intensity 2 ×TA	/a.u. A(TO)	E(TO)	E(LO)	TA + LO	A(TO)/E(TO)	Position/cm ⁻¹ LO
ZnS:Gd0	0.608	0.546	0.198	0.133	0.089		346.336
ZnS:Gd0.1	0.723	0.398	0.597	0.161	0.270	0.667	346.956
ZnS:Gd0.3	0.699	0.271	0.702	0.181	0.280	0.386	347.801
ZnS:Gd0.5	0.731	0.621	0.425	0.162	0.292	1.461	345.439
ZnS:Gd0.7	0.702	0.598	0.434	0.157	0.271	1.378	345.498
ZnS:Gd1.0	0.641	0.492	0.348	0.129	0.189	1.414	345.465

The crystalline phase of the synthesized ZnS and ZnS:Gd samples was evaluated using XRD. Fig. 1(c) presents the diffractograms of all samples, indexed according to the crystallographic planes of the sphalerite structure, which crystallizes in the cubic F-43 m space group (DB card No. 01-080-4383). No secondary phases were observed. The broad peaks in each case indicate that the crystallite size of all samples is relatively small; the mean crystallite size, calculated by the Williamson–Hall method, is 2 nm, with no differences between the undoped and doped samples. The smaller crystal size provides

more active sites for absorbing ions, which is beneficial for storing charges [38].

The surface functional groups of the synthesized particles were determined by FT-IR spectroscopy. Fig. 1(d) shows the FT-IR spectra of undoped and Gd-doped ZnS samples. Ideally, the spectrum should contain almost no signals except for a small band denoting the Zn-S bonds. This band is visible in all spectra of both doped and undoped samples at $\approx 642~\rm cm^{-1}$ [39]. All spectra also contain a broad band between 3000–3500 cm⁻¹, denoting $\nu(O-H)$ vibrations, which stem from the surface of the nanoparticles, where OH groups may exchange

I. Nesterovschi et al.

some of the sulfide. Since the particle size is rather small, this band is relatively large compared to other samples of ZnS. Interestingly, some bands can be observed at 1621 and 1400–1520 cm $^{-1}$. In this region, generally, $\nu(\text{C=O})$ is supposed to be visible, which normally comes from organic coatings [40]. Since no organic compound was used in this case, another possible explanation could be the sorption of CO $_2$, which could adsorb physically or chemically as carbonate or hydrogen carbonate.

UV–VIS spectroscopy was conducted to evaluate the sample's optical properties, and the obtained absorption spectra are shown in Figure S-UV–vis*. A broad absorption range from 200 to 410 nm is observed for all samples. The absorption edge of the Gd-doped samples shows a redshift relative to the undoped ZnS sample. The absorption spectra were utilized to determine the band gap energy. As presented in Figure S-Tauc*, the values of the band gap were determined from the plot of $(\alpha h v)^2$ versus h v, by extrapolating the linear portion of the graph to the x-axis, as indicated by the Tauc relation, and the obtained values are inserted in the figure inset. The band gap energy of the undoped ZnS is 3.50 eV, consistent with values reported in the literature for ZnS materials with a cubic structure [41]. Doping reduces the energy band gap, which is attributed to the formation of impurity levels from the Gd 4f electronic state within the ZnS band gap [42,43], facilitating the charge transfer and favoring electrical conductivity [44].

More insights regarding the defect states and charge carrier recombination were obtained by PL spectroscopy. The spectra obtained under an excitation wavelength of 320 nm are shown in Fig. 2(a), and the emission bands are quite similar. By doping with Gd ions, the intensity of the PL spectra is quenched, suggesting that Gd 4f energy levels become electron traps, better separating the electron–hole pairs, thus delaying the recombination process [45]. The PL spectra were deconvoluted into 4 bands using a multiple Gaussian peak function to analyze the emission-related transitions. For example, Fig. 2(b) illustrates the deconvolution of the PL spectrum corresponding to the ZnS:Gd0.3 sample, while the other deconvolutions are presented in Figure S-PL*(a–d). Table 1 summarizes the results related to the relative area of the peaks obtained after the spectra deconvolution. The relative area represents the ratio between the specific band area and the total spectrum area.

Previous studies report that vacancies occupy deeper states in the gap compared with those of interstitial atoms [46]. Thus, the bands specific to the interstitial position appear at higher energy, and those corresponding to a vacancy at lower energy. The position in the band gap of the Zn and S states (interstitial or vacancy) depends on the size of the respective atoms and was explained in the Ref. [47]. Thus, the bands centered at 410 nm and 433 nm were attributed to S_i , Zn_i , while those at 458 nm and 503 nm correspond to V_S and V_{Zn} , respectively.

Analysis of the relative band areas from the spectral deconvolution reveals that Gd doping reduces sulfur vacancies but increases interstitial sulfur defects compared to the undoped sample. In the case of Zn, the vacancies are decreasing, meaning that Gd ions enter the ZnS lattice. However, the interstitial Zn defects are increasing since some Zn ions are replaced by Gd ions, creating strain in the crystal structure.

More structural information about the samples was obtained by Raman spectroscopy. The spectra are shown in Fig. 2(c). The Raman spectra of Gd-doped ZnS exhibit six primary bands. The peak at 133 cm $^{-1}$ corresponds to the overtone of the transverse acoustic (TA) mode (2 \times TA), with its intensity affected by sulfur vacancies. An increased Raman intensity at this position indicates a higher concentration of sulfur vacancies [48]. The transverse optical (TO) mode at 260 cm $^{-1}$ is associated with dopant incorporation, as indicated by a redshift. This redshift reflects an increase in the dopant concentration within the lattice [49,50]. The longitudinal optical (LO) mode at 345 cm $^{-1}$ is influenced by interstitial sulfur, where a redshift suggests an increased concentration of interstitial sulfur defects [48]. Additional peaks appear at 427 cm $^{-1}$, 646 cm $^{-1}$, and 987 cm $^{-1}$. The 427 cm $^{-1}$ band corresponds to the second-order TA + LO mode, while

the 646 cm⁻¹ band is attributed to $2 \times LO$, overlapping with the LO + TO mode. The 987 cm⁻¹ peak is assigned to $3 \times LO$ [51,52].

Comparing pristine ZnS and Gd-doped samples reveals several visible differences. The pristine sample exhibits a lower relative intensity at 427 cm⁻¹ and lacks the 1012 cm⁻¹ shoulder observed in the doped samples. The presence of this shoulder in the doped samples indicates that this band is activated by the dopant (Fig. 2(c)). It is probably an overtone linked to defect-related enhancement near the TO mode at 255 cm⁻¹, and can be assigned to the A(TO) vibrational mode [48, 53,54]. While no significant spectral differences are observed among the doped samples in the spectra, deconvolution of the Raman spectra using a multiple-Gaussian function reveals subtle variations, and a representative example is presented in Figure S-Raman*.

As presented in Table 2, the deconvolution results reveal significant variations in the intensities of the second-order TA mode and the TA + LO mode. Specifically, the intensity increases up to the sample ZnS:Gd0.5, suggesting that this sample contains the highest sulfur vacancy concentration following PL results. A change is also observed in the TO mode, representing dopant incorporation into the lattice. After deconvolution, the TO mode is separated into two bands, located at 255 cm⁻¹ and 265 cm⁻¹, corresponding to the E(TO) and A(TO) modes of vibration, respectively. The Raman shift of the TO mode can be correlated to the dopant concentration in the lattice: it can be observed that the relative intensity between the A(TO) and E(TO) modes is decreasing by Gd doping, meaning that Gd ions occupy the Zn vacancy sites. As illustrated in Table 2, the sample ZnS:Gd0.3 exhibits the lowest relative intensity, suggesting the highest gadolinium incorporation in the lattice.

Furthermore, although the LO mode is mainly affected by the concentration of interstitial sulfur, no significant shifts in its position are detected beyond the 1 cm $^{-1}$ spectral resolution. However, after deconvolution, an additional peak is detected corresponding to the LO mode at 319 cm $^{-1}$. This peak corresponds to the E-symmetry component of the LO vibrational mode [48]. The intensity of this peak fluctuates, causing a shift in the overall LO Raman band. Increased intensity results in a noticeable redshift of the LO band, similar to the TO mode. Thus, the E(LO) mode intensity is linked to the concentration of interstitial sulfur. It can be observed that the intensity of this band increases by doping until a nominal concentration of 0.3% Gd followed by a slightly decrease.

The room temperature Q-band EPR spectra of undoped and doped ZnS with different concentrations of Gd are shown in Fig. 2(d). The EPR method is a suitable tool to probe the existence of Gd³⁺ ions because its ground state, ${}^{8}S_{7/2}(4f^{7})$, has L = 0. Therefore, its long relaxation time enables it to be detected at room temperature. In the undoped ZnS sample, defects such as monoionized Zn vacancies (VZn) and S vacancies (V_S) can exist, both of which are EPR active. The pristine ZnS spectrum shows a strong isotropic signal with g = 2.003, which is attributed to defects in the crystalline structure of the material, representing V_S [55]. By doping, the intensity of these signals increases, and at the same time, two new EPR resonances appear, one with g = 2.0045 and a second with g = 1.992. As described previously [55,56], V_{Zn} resonances appear in the g = 2.0035 to 2.075 range. We attribute the second EPR resonance to Gd³⁺ centers doped into the ZnS structure. This signal increases in intensity with the Gd-dopant concentration, and several works report almost identical g-values for these centers in cubic structures [57-59]. Thus, doping ZnS with Gd ions introduces not only Gd3+ ions into the ZnS lattice but also increases the concentration of monoionized Zn- and S-related vacancy sites.

All the EPR spectra of the Gd-doped ZnS particles measured in the Q-band show an additional signal with a hyperfine characteristic of Mn²⁺ impurity (see with '*' marked signals in Fig. 2(d)) from the synthesis process that does not change in intensity. The relatively weak resonances are unavoidable since an exactly pure sample cannot be technically prepared. Still, an ultra-high sensitive spectroscopy method like EPR can detect even such a low-concentrated impurity signal.

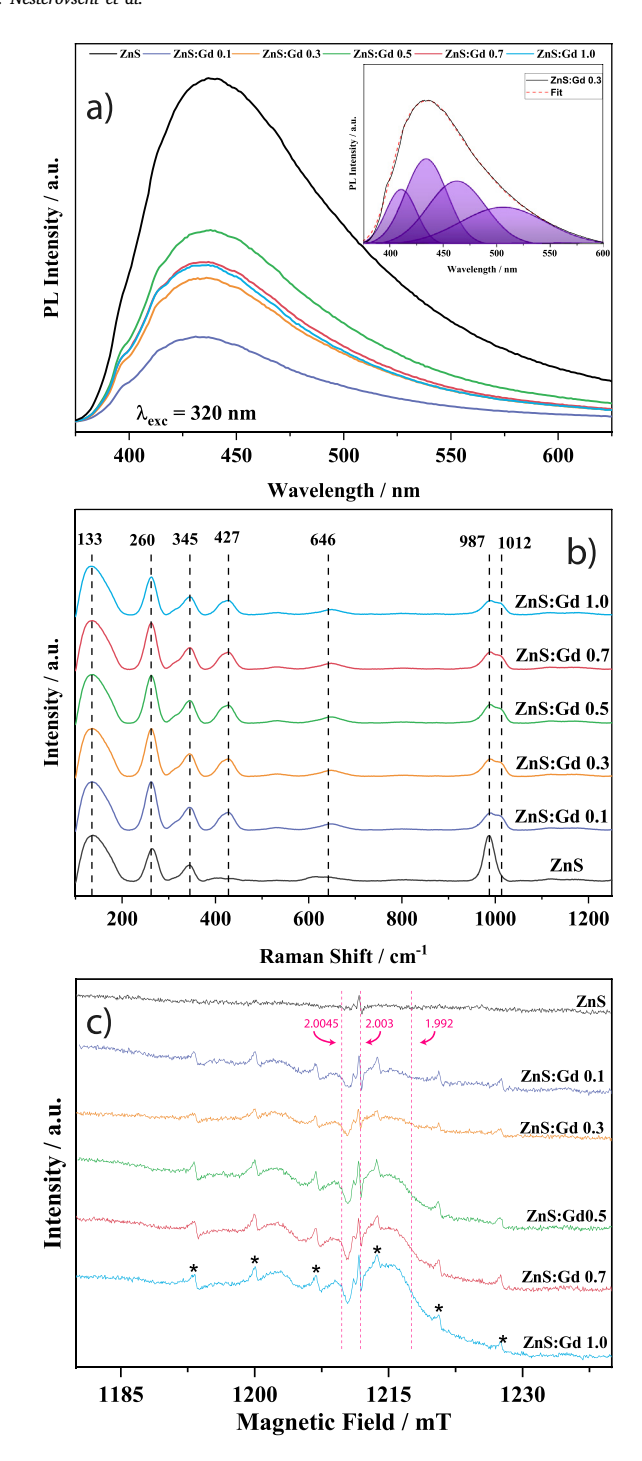


Fig. 2. PL spectra of the undoped and Gd-doped ZnS materials, where the inset presents the Gaussian deconvolution of the ZnS:Gd0.3 PL spectrum (a), as well as Raman (b) and EPR spectra (c) of all ZnS-based samples.

The textural properties of the samples were evaluated from the N_2 sorption isotherms. All samples show a type IV isotherm with a H2(a) type hysteresis loop (Figure S-BET*) characteristic of ordered mesoporous materials [60].

The electrodes' mesoporous configuration enables rapid electrolyte insertion by fewer diffusion routes of OH⁻ and enhances the electroactive regions for ion transport [61]. Indeed, all samples show a narrow pore size distribution centered around 3 nm. The ZnS samples' specific surface area and pore volume are listed in Table 3. It may be noticed that the Gd-doped ZnS samples exhibit twice as large specific surface

Table 3 Textural properties of the samples. ^a BET specific surface area calculated in the $0.02 - 0.25 \ p/p_0$ range. ^b Total pore volume calculated at p/p_0 =0.95.

Sample	$S_{BET}^a/\mathrm{m}^2/\mathrm{g}$	$V_p^b/\mathrm{cm}^3/\mathrm{g}$
ZnS:Gd0	66.1	0.066
ZnS:Gd0.1	112.8	0.108
ZnS:Gd0.3	127.4	0.116
ZnS:Gd0.5	106.0	0.105
ZnS:Gd0.7	113.2	0.108
ZnS:Gd1.0	110.8	0.110

area values and pore volumes as compared to the undoped ZnS. However, there is not any clear dependence between the Gd doping amount and the values of the textural properties. Enhancement of surface area and pore volume due to Gd doping favors mass and charge transport, positively influencing the electrochemical processes [62].

The electrochemical performance of the synthesized samples was tested in all-in-one symmetric supercapacitor devices, where 6 M KOH served as the electrolyte and glass fiber was used as the separator material. Fig. 3(a) depicts the cyclic voltammetry curve for all the assembled devices, measured at 100 mV/s within the 0-1 V voltage window. The current value increased as the Gd dopant percentage increased until it reached a maximum, and then the current value decreased. ZnS:Gd0.5 has the highest current value; after that, the increase in dopant percentage tends to reduce the current values. The undoped ZnS own the lowest current, highlighting that Gd doping facilitates faster charge transport. The shape of the CV curves provides valuable information about which phenomenon dominates the charge storage process. Figure S-CV* illustrates the CV curves for all devices measured at different scan rates, giving a detailed insight into the rate capability and reversibility. Fig. 3(a) and S-CV* prove that the undoped ZnS based device presents a pseudocapacitance-dominated CV curve where the redox peaks at each scan rate are visible. Still, the drop in peak current value is prominent as we move towards lower scan rates, suggesting low rate capability. The ZnS:Gd0.1 device shows a non-ideal CV curve with significant deviation from an EDLC-type rectangular curve; the redox peaks disappear for this device, demonstrating that the EDLC phenomenon started to influence the charge storage process, although the current values do not show any significant change. From all CV curves measured at different scan rates of ZnS:Gd0.1 results an improvement in the rate capability of the device compared to the undoped ZnS device, as there is no sharp drop in peak current values. At higher nominal Gd-dopant percentages (0.3, 0.5, 0.7, and 1%), similar CV curve types with differences in current values and area under the CV curve were observed. All these devices present a non-ideal quasi-rectangular curve, which hints slight deviation from rectangular EDLC-type CV. The curve shifts from an ideal rectangular shape in practical devices due to the components' internal resistance and surface faradaic reaction. The rounding of CV curves edges at the corners in real supercapacitor devices due to the resistance among components, and the sudden spike in current values at peak voltage, is linked to faradaic reactions [63,64]. The ZnS:Gd0.5-based SC device shows the highest current value, followed by ZnS:Gd0.7 and then ZnS:Gd0.3. From the rate capability of these devices, shown in Figure S-CV* and 3(b), results a gradual drop in the peak current values.

Fig. 3(b) depicts the specific capacitance (C_s) measured with CV at different scan rates using the following equation: $C_s = \frac{\int_{V_1}^{V_2} I(V) \mathrm{d}V}{2\ mK \, dV}$, where $\int_{V_1}^{V_2} I(V) \mathrm{d}V$ represents the area under the CV curve, m is the mass of active electrode material, K is the scan rate at which the CV was acquired and ΔV is the voltage window. The ZnS:Gd0.5-based SC device has the highest C_s value at each scan rate, with the maximum being 114.70 F/g at 2 mV/s. The C_s values have an increasing trend with the nominal Gd concentration until 0.5%, after which the C_s values start

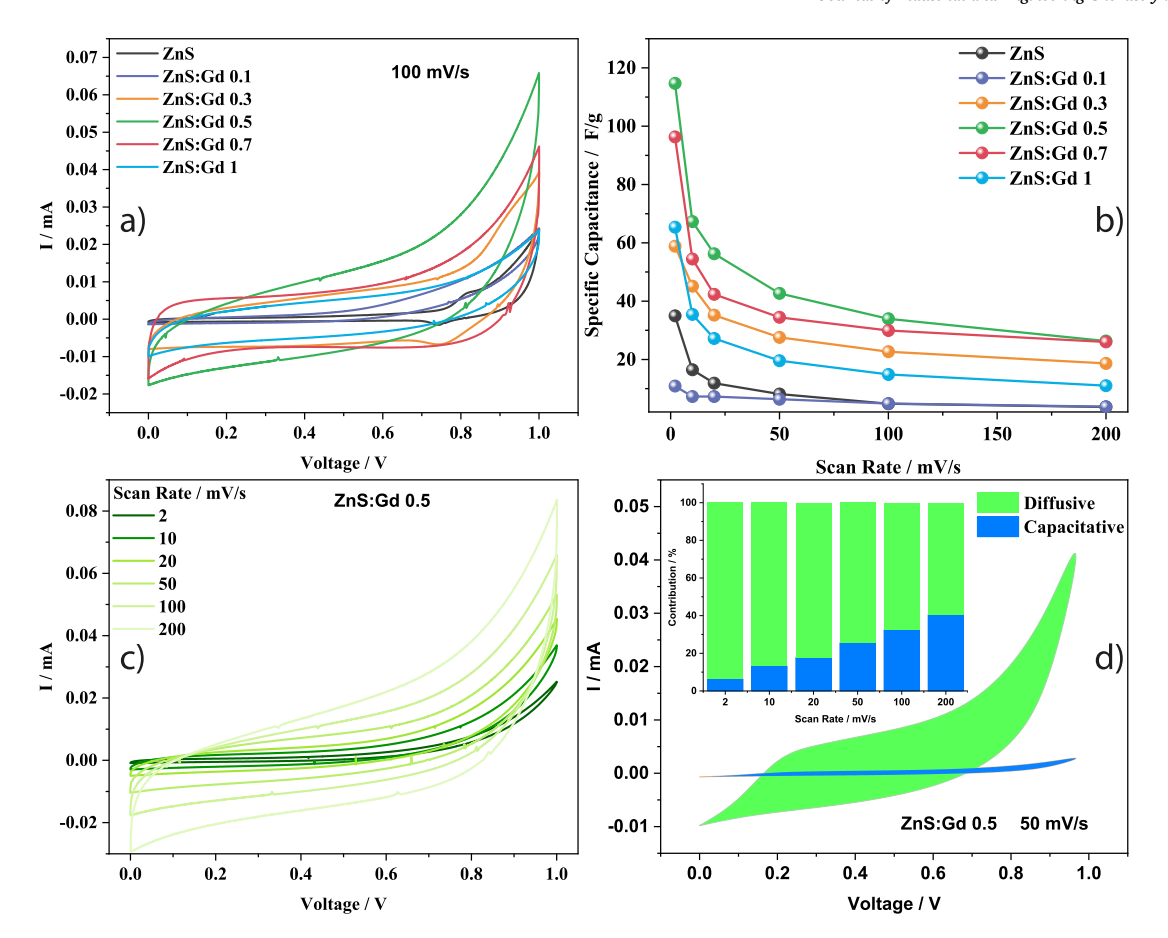


Fig. 3. CV results measured at 100 mV/s for the ZnS:Gd samples (a), Specific capacitance as a function of the CV scan rate (b), CV measured at different scan rates (c), and Dunn analysis (d) for ZnS:Gd0.5 sample.

Table 4 R_1 , the solution resistance (R_s) , R_2 , the charge transfer resistance (R_{cl}) , and the double-layer capacitance C_{dl} values obtained with the equivalent circuit fit of the Nquist plots of the undoped and Gd-doped ZnS based supercapacitors, as well as the energy E_D and power P_D density values calculated from Csp at 2mV/s.

Sample	R_1	C_{dl}	R_2	Csp	E_D	P _D
	$/\Omega$	/μF	$/\Omega$	/F/g	/Wh/kg	/ W/kg
ZnS	120	5.64	8970	34.96	4.85	349
ZnS:Gd0.1	172	3.80	2234	10.86	1.50	108
ZnS:Gd0.3	10.21	66.72	608	58.87	8.17	588
ZnS:Gd0.5	6.23	63.27	4.518	114.70	15.93	1146
ZnS:Gd0.7	1.75	126	1863	96.33	13.38	963
ZnS:Gd1.0	13	13.21	8841	65.34	9.075	653

declining, indicating a dopant saturation point, considering the charge storage properties.

To get further insights into the working mechanism of the best-performing ZnS:Gd0.5 based device, Dunn analysis was applied [65]. The equation used to express the different contributions to the measured current is expressed as $I(V) = k_1 \cdot v + k_2 \cdot \sqrt{v}$, where $k_1 \cdot v$ represents the capacitive current, $k_2 \cdot \sqrt{v}$ and v are the diffusive current, and the scan rate, respectively. The relative contributions of each mechanism can be determined by examining the slope and intercept of a Dunn plot, corresponding to the constants k_1 and k_2 . Fig. 3(d) illustrates the Dunn plot, and in the inset, the diffusive and capacitive contributions at various scan rates are presented. It is observed that the diffusive phenomenon dominates at all scan rates, suggesting that redox contribution plays a major role in charge storage, as mentioned in the CV section. The diffusive contribution increases at lower scan

rates, as ions have more time to penetrate the bulk of the material. The contributions at 50 mV/s are plotted as parts of the CV curve - Fig. 3(d), showing the major share of the diffusive process [66].

Electrochemical impedance spectroscopy (EIS) is another widely used technique for characterizing electrochemical devices, providing insights into the impedance associated with these devices. Fig. 4(a) presents the Nyquist plot for all supercapacitor devices, a method for representing EIS data where the negative imaginary impedance is plotted against the real impedance. Fig. 4(a) illustrates that all devices yield an incomplete semicircle. The inset shows a zoomedin view of the high-frequency region, offering information on the solution resistance (R_s) and charge-transfer resistance (R_{ct}) . The xintercept in the high-frequency region corresponds to R_s , which reflects the inherent electrolyte-electrode resistance and significantly impacts electrochemical performance [67,68]. As illustrated in the inset of Fig. 4(a), no extra semicircle is observed in the high-frequency region for any of the devices; this semicircle is linked to R_{ct} , and its absence suggests a low R_{ct} value [69]. Undoped ZnS and ZnS: Gd1.0 show higher R_s values, consistent with the CV results, which may explain the lower current values observed in the CV measurements. W represents the Warburg impedance, which is the ion diffusion limitation at the electrode/electrolyte interface and ideally represented by a 45-degree line at low frequency. The steeper the line at low frequency, the slower the ion diffusion, and this affects the electrochemical performance of the device.

Samples with moderate Gd doping display a decreased R_s , indicating improved charge flow with reduced resistance in these devices. The top-performing devices ZnS:Gd0.5, ZnS:Gd0.7, and ZnS:Gd0.3 exhibit the smallest semicircle diameters, indicating lower values on both the imaginary and real axes. To further analyze the circuits and obtain

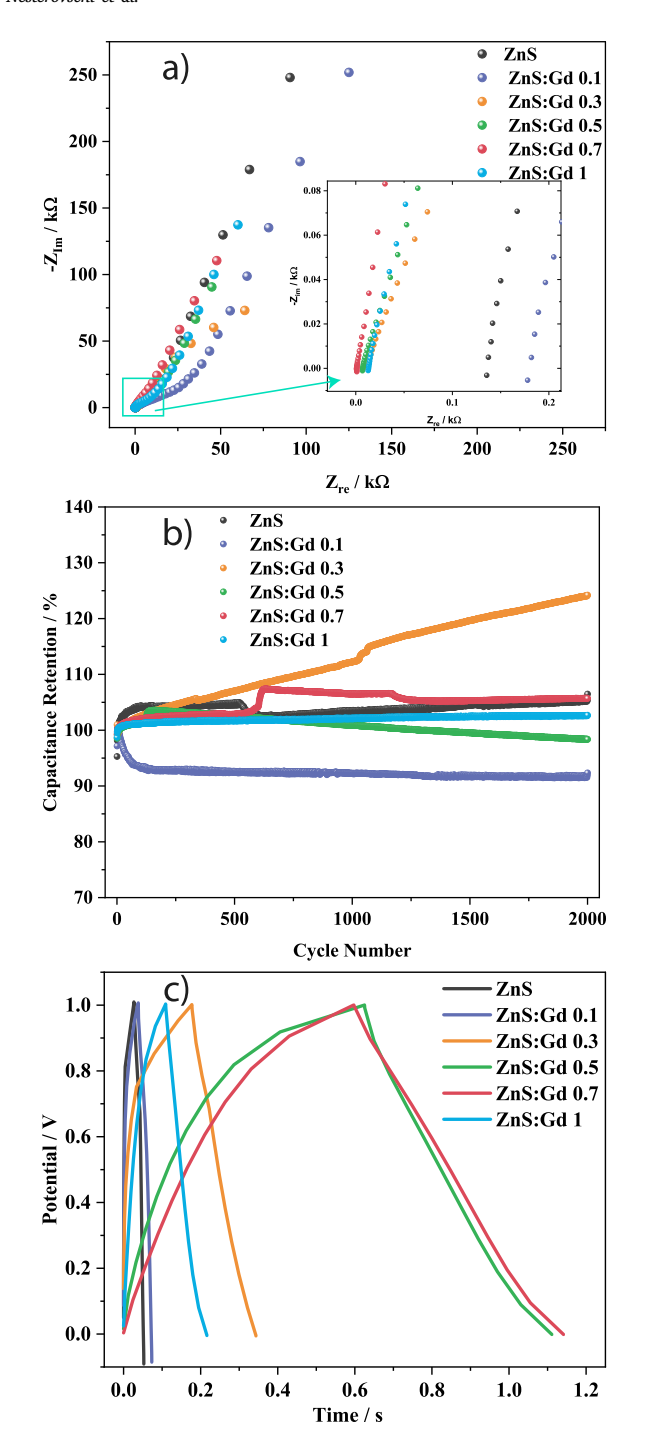


Fig. 4. Nyquist plot where the inset shows a zoom-in on the high-frequency region (a), Capacitance Retention as a function of the cycle number (b), and GCPL curves measured at 0.8 A/g in the voltage window of 0–1 V for all ZnS:Gd samples used as electrode materials for supercapacitors.

values of the physical parameters in Nyquist plots, equivalent circuit fitting was performed. The fitted plots and the equivalent circuits used for fitting are shown in Figure S-PEIS*. The values of the component are shown in Table 4. The equivalent circuit elements are described as follows: R_1 is the solution resistance (R_s), R_2 is the charge transfer resistance (R_{cl}), Q shows a constant phase element (CPE), which is a more generalized impedance element that accounts for non-idealities in the capacitor's behavior, Q_1 in the circuit is analogous to C_{dl} which is the double-layer capacitance, C_2 or Q_2 represents a pseudo-capacitance

Table 5 C_s , E_D , and P_D values of supercapacitor devices using electrode materials based on doped ZnS already reported in the literature compared to the ones reported in this study. Abbreviations: sym — symmetric, asym — asymmetric, NT — nanotubes, AC — active carbon, t.w. — this work.

Material	SC type	$C_s/F/g$	E_D /Wh/kg	$P_D/W/kg$	Ref.
ZnS:Mn	asym - AC	1905 @ 1 A/g	43.3	6800	[27]
ZnS:Fe	asym - AC	700 @ 1 A/g	11	591.2	[31]
ZnS:Mo	asym - AC	2208 @ 1 A/g	26.5	1303	[70]
Zns:Ni	asym - Pt	223 @ 10 mV/s	-	-	[71]
ZnS:Co	sym	947.8 @ 10 mV/s	-	-	[30]
ZnS:Cu	sym	743 @ 1 A/g	_	_	[72]
ZnS:C NT	sym	347.3 @ 0.5 A/g	22.3	500	[73]
ZnS:Gd0.5	sym	114.7 @ 2 mV/s	15.9	1146	t.w.

(which was also discussed in the CV section), W mean the Warburg impedance from ion diffusion in the electrolyte at a low-frequency region, R_3 represent the diffusion or additional interfaces resistance depending on the attached component and L1 component present in the ZnS:Gd0.7 based device at high frequency region is associated with stray inductance generate in cell cables and appears in the positive imaginary impedance. The values of R_s , R_{ct} and C_{dl} are shown in Table 4. Undoped ZnS and ZnS:Gd1 samples have the highest values of R_s and R_{ct} and low value of C_{dl} , while the best performing ZnS:Gd0.5 sample owns low values of R_s and R_{ct} along with highest value of C_{dl} in line with the previously obtained results. The absence of a well-defined Warburg region in the Nyquist plots may be attributed to the fast ion transport and capacitive behavior of the Gd-doped ZnS electrodes (as shown in the CV curve that increased Gd doping tends to shift the CV more to the rectangular side and redox bumps are removed, which shows increased EDLC behavior). In two-electrode symmetric configurations, especially when using materials with nanostructure, high conductivity, and defective structure, diffusion limitations become minimal, leading to a direct transition from the charge-transfer semicircle to a nearly vertical low-frequency line, which indicates that a transition from diffusion-limited kinetics in the undoped sample to surface-controlled capacitive behavior in doped electrodes, attributed to enhanced conductivity and improved ion accessibility due to Gd

Fig. 4(b) illustrates the cyclic stability of all devices by plotting capacitance retention against cycle number. All the devices exhibit excellent retention values, with a slight decrease in the capacitance retention values after 2000 cycles. This highlights the exceptional cyclic stability for this type of electrode material. Fig. 4(c) presents the galvanostatic charge–discharge curve measured at 0.8 A/g, showing that ZnS:Gd0.5 and ZnS:Gd0.7 based devices have the longest discharge time, while the undoped ZnS and ZnS:Gd0.1 exhibit the lowest discharge time. The charge–discharge results show the same trend observed in the CV and PEIS results. In the case of the best-performing devices, a small plateau region at the peak voltage associated with the faradaic reaction in the device appears [74,75].

The energy and power density values are a standard metric for comparing energy storage devices, popularly known as the Ragone plot. All devices' energy and power density values measured from the best specific capacitance value using equation S-E1* and S-E2* are presented in Table 4 to compare the electrochemical performance of the supercapacitor devices. ZnS:Gd0.5-based device shows the highest energy and power density values, followed by ZnS:Gd0.7-based device. The undoped ZnS based device has the lowest performance, a trend followed in all the electrochemical results. The enhancement in electrochemical characteristics of ZnS by doping with Gd ions can be explained since doping with Gd ions generates, besides the new energy levels of Gd 4f electronic state, also different defect states like interstitial and vacancy of Zn and S, as evidenced by PL, Raman, and EPR spectroscopy. All these energy levels act as additional ion

I. Nesterovschi et al.

diffusion pathways and electrochemically active sites [76]. This enhancement was anticipated, as all doped samples possess a narrower energy band gap than ZnS, which promotes charge transfer and allows more efficient electrical conduction via free carriers. Moreover, the best supercapacitor performance sample, ZnS:Gd0.5, shows the highest sulfur vacancy concentration as shown in the PL and Raman results. These vacancies act as electrochemically active sites, facilitating ion adsorption and improving charge storage [77]. V_{Zn} and V_S create localized states within the ZnS band gap. These vacancies are electrochemically active sites, facilitating ion adsorption and redox reactions at the electrode-electrolyte interface. The redox peaks observed in the CV curves of undoped and doped ZnS are attributed to defectinduced faradaic reactions involving surface Zn and S vacancies and electrochemically active hydroxyl species from the electrolyte. A higher density of such sites increases the pseudocapacitive contribution, as confirmed by the strong diffusion-controlled behavior in Dunn analysis. The introduction of Gd^{3+} alters the electronic structure by creating shallow donor levels and reducing the bandgap. Defect-related energy states trap electrons, delaying electron-hole recombination (supported by PL quenching), which prolongs carrier lifetimes and improves conductivity. This enhanced conductivity enables faster electron transfer during charge-discharge cycles. The decrease in specific capacitance values after increasing the nominal Gd doping content from 0.5% is a commonly observed trend in supercapacitor research. This behavior can be explained by the fact that moderate Gd doping may introduce additional active sites and increase the electrical conductivity of the ZnS matrix. In contrast, after reaching a certain optimized value, further increase in dopant content decreases the performance of the device; this decline can be attributed to the excessive Gd causing crystal defects, grain boundary formation, and possible particle agglomeration, all of which may reduce the available surface area for charge storage. Additionally, high Gd concentrations can act as recombination centers for charge carriers, reducing conductivity.

Table 5 compares the best-performing electrode material's electric properties studied in this work with previously reported works where ZnS was used as an electrode material with different dopants in supercapacitor applications. The comparison highlights the capability of Gd-doped ZnS developed here as symmetric devices without using a carbon-based booster material for supercapacitor applications. In this work, we used a two-electrode system for electrode measurement to test the whole device rather than only the electrode material from a three-electrode system, which always shows a high specific capacitance value compared to the two-electrode system. In this regard, this table is provided to contextualize the performance of our Gd-doped ZnS electrode among similar ZnS-based or rare-earth doped systems.

Conclusions

Gd-doped zinc sulfide samples were synthesized using a precipitation reaction method. The morphology of the samples was analyzed using STEM measurements, which show that the particles aggregate into larger layered structures with sharp edges. EDS confirmed the homogeneous presence of Gd dopant ions across the ZnS particles. All samples exhibit a sphalerite crystalline structure determined by XRD, with broad diffraction peaks indicating very small average crystallite sizes. The band gap energy of the samples narrows by doping, which is beneficial for the charge transfer, enhancing electrical conductivity. This reduction in the band gap is due to the formation of impurity levels in the ZnS gap from doping, which was further confirmed by PL measurements that indicate quenching due to Gd ions, as the Gd 4f energy levels become electron traps, enhancing the separation of electronhole pairs. Additionally, PL analysis revealed bands corresponding to interstitial and vacancy sites of sulfur and zinc, respectively. The analysis of these bands reveals that Gd doping results in some Zn ions being replaced by Gd ions, with excess Zn remaining in the interstitial position. Raman spectroscopy demonstrated that incorporating Gd ions

into the ZnS lattice induced a higher concentration of sulfur defects, while EPR spectroscopy highlighted the presence of mono-ionized Znand S-related vacancies and Gd3+ sites. By Gd doping, the specific surface area values and pore volumes increase twice compared to ZnS particles. All-in-one symmetric supercapacitor devices were used to evaluate the electrochemical performance of the synthesized samples. The CV results suggest that charge storage occurs through double-layer and pseudo-capacitance mechanisms. The ZnS:Gd0.5 sample exhibits the highest specific capacitance value at each scan rate, reaching a maximum of 114.70 F/g at 2 mV/s. Dunn's analysis indicates that the diffusive phenomenon dominates the energy storage mechanism, suggesting that redox processes play a significant role in charge storage. PEIS results show that the ZnS:Gd0.5 sample has the lowest charge flow resistance. All devices demonstrate good cyclic stability, with the bestperforming material, ZnS:Gd0.5, exhibiting excellent cyclic stability, retaining about 98% after 2000 cycles. When examined in terms of energy and power density values, standard metrics for comparing energy storage devices, the best-performing ZnS sample nominally doped with 0.5% Gd ions demonstrates excellent values of 15.93 Wh/kg and 1146 W/kg, respectively. These results underscore the potential of ZnS materials doped with rare earth metals like Gd in the energy storage field, particularly in supercapacitors, when employed as electrode materials.

CRediT authorship contribution statement

Ion Nesterovschi: Writing - review & editing, Writing - original draft, Visualization, Investigation, Formal analysis. Ameen Uddin Ammar: Writing - review & editing, Writing - original draft, Validation, Methodology, Investigation, Formal analysis. Alexander Bunge: Writing - review & editing, Writing - original draft, Investigation, Formal analysis. Adriana Popa: Writing - review & editing, Writing - original draft, Investigation, Formal analysis, Data curation. Maria Stefan: Writing - original draft, Investigation, Formal analysis. Sergiu Macavei: Investigation, Formal analysis. Iolanda Ganea: Investigation, Formal analysis. Marin Senila: Investigation, Formal analysis. Emre Erdem: Writing - review & editing, Writing - original draft, Visualization, Validation, Supervision, Formal analysis. Arpad Mihai Rostas: Writing - review & editing, Writing - original draft, Visualization, Validation, Supervision, Investigation, Formal analysis, Data curation, Conceptualization. Dana Toloman: Writing - review & editing, Writing - original draft, Validation, Supervision, Investigation, Formal analysis, Conceptualization.

Declaration of competing interest

The authors declare that they have no known competing financial interests or personal relationships that could have appeared to influence the work reported in this paper.

Acknowledgments

The authors would like to express appreciation for the financial support of the Ministry of Research, Innovation and Digitalization, Romania's National Recovery and Resilience Plan, PNRR-III-C9-2022-I8, CF 163/15.11.22, financing contract no. 760097/23.05.23. Also, the authors are grateful to Maria Mihet for conducting the BET measurements.

Supplementary data

Supplementary material related to this article can be found online at https://doi.org/10.1016/j.jiec.2025.09.014.

Data availability

Data will be made available on request.

References

- [1] M. Amir, R.G. Deshmukh, H.M. Khalid, Z. Said, A. Raza, S. Muyeen, A.-S. Nizami, R.M. Elavarasan, R. Saidur, K. Sopian, Energy storage technologies: An integrated survey of developments, global economical/environmental effects, optimal scheduling model, and sustainable adaption policies, J. Energy Storage 72 (2023) 108694.
- [2] M. Sadiq, N. Drissi, K. Tahir, A. Kumar, Fabrication of agglomerated WSe2-based rGO nanocomposite via a novel hydrothermal procedure for an energy conversion application, Diam. Relat. Mater. 153 (2025) 112002.
- [3] M. Abdullah, P. John, K. Jabbour, M.I. Ahmad, S. Khan, M.S. Waheed, M.D. Albaqami, M. Sheikh, M.F. Ehsan, M.N. Ashiq, Improvement in capacitive performance of ZnS with MnO2 via composite (Zns/MnO2) strategy developed by hydrothermal technique, J. Energy Storage 78 (2024) 110034.
- [4] S. Sharma, P. Chand, Supercapacitor and electrochemical techniques: A brief review, Results Chem. 5 (2023) 100885.
- [5] M. Abdullah, P. John, S. Manzoor, M.I. Ghouri, H. Hegazy, A.H. Chugtai, S. Aman, A.M. Shawky, M.N. Ashiq, T. Taha, Facile fabrication of CuO/Ag2Se nanosized composite via hydrothermal approach for the electrochemical energy conversion system, J. Energy Storage 56 (2022) 105929.
- [6] R.T. Yadlapalli, R.R. Alla, R. Kandipati, A. Kotapati, Super capacitors for energy storage: Progress, applications and challenges, J. Energy Storage 49 (2022) 104194.
- [7] H.R. Khan, A.L. Ahmad, Supercapacitors: Overcoming current limitations and charting the course for next-generation energy storage, J. Ind. Eng. Chem. (2024).
- [8] M. Aadil, A.G. Taki, S. Zulfiqar, A. Rahman, M. Shahid, M.F. Warsi, Z. Ahmad, A.A. Alothman, S. Mohammad, Gadolinium doped zinc ferrite nanoar-chitecture reinforced with a carbonaceous matrix: a novel hybrid material for next-generation flexible capacitors, RSC Adv. 13 (40) (2023) 28063–28075.
- [9] Y. Ejaz, B. Alotaibi, A.W. Alrowaily, H.A. Alyousef, H. Somaily, S. Aman, Development of cost-efficient BaMnO3/rGO nanocomposite as electrode for energy storage applications in supercapacitor, Ceram. Int. 50 (15) (2024) 27508–27519.
- [10] M. Pathak, D. Bhatt, R.C. Bhatt, B.S. Bohra, G. Tatrari, S. Rana, M.C. Arya, N.G. Sahoo, High energy density supercapacitors: an overview of efficient electrode materials, electrolytes, design, and fabrication, Chem. Rec. 24 (1) (2024) e202300236.
- [11] Z. Ahmad, W. Kim, S. Kumar, T.-H. Yoon, J.-S. Lee, Nanocomposite supercapacitor electrode from sulfonated graphene oxide and poly (pyrrole-(biphenyldisulfonic acid)-pyrrole), ACS Appl. Energy Mater. 3 (7) (2020) 67342 6751
- [12] M. Ashan, F. Alharbi, S. Aman, A.G. Al-Sehemi, K. Ahmad, M. Aslam, M.I. Saleem, Elevating capacitive features of hydrothermally produced CeVS3 utilizing rGO for supercapacitor applications, Diam. Relat. Mater. 147 (2024) 111319.
- [13] Z. Ahmad, S. Kumar, C.K. Trinh, J.-J. Shim, J.-S. Lee, Decoupling electrochemical parameters of molecular-level-controlled polypyrrole and graphene oxide nanocomposite, Appl. Surf. Sci. 610 (2023) 155464.
- [14] Z. Ahmad, W.-B. Kim, S. Kumar, T.-H. Yoon, J.-J. Shim, J.-S. Lee, Redoxactive supercapacitor electrode from two-monomer-connected precursor (pyrrole: Anthraquinonedisulfonic acid: Pyrrole) and sulfonated multi-walled carbon nanotube, Electrochim. Acta 415 (2022) 140243.
- [15] D.A. Alshammari, I.A. Ahmed, S.D. Alahmari, M. Abdullah, S. Aman, N. Ahmad, A. Henaish, Z. Ahmad, H.M.T. Farid, Z.M. El-Bahy, Electrochemical investigation of niobium doped nickel selenide nanostructure for supercapacitor devices, J. Energy Storage 75 (2024) 109886.
- [16] P. Forouzandeh, V. Kumaravel, S.C. Pillai, Electrode materials for supercapacitors: a review of recent advances, Catalysts 10 (9) (2020) 969
- [17] L. Phor, A. Kumar, S. Chahal, et al., Electrode materials for supercapacitors: a comprehensive review of advancements and performance, J. Energy Storage 84 (2024) 110698.
- [18] D. Toloman, A. Gungor, A. Popa, M. Stefan, S. Macavei, L. Barbu-Tudoran, A. Varadi, I.D. Yildirim, R. Suciu, I. Nesterovschi, et al., Morphological impact on the supercapacitive performance of nanostructured ZnO electrodes, Ceram. Int. 51 (1) (2025) 353–365.
- [19] M.A. Dar, S. Majid, M. Satgunam, C. Siva, S. Ansari, P. Arusalan, S.R. Ahamed, Advancements in supercapacitor electrodes and perspectives for future energy storage technologies, Int. J. Hydrog. Energy 70 (2024) 10–28.
- [20] M. Stefan, E.-J. Popovici, O. Pana, E. Indrea, Synthesis of luminescent zinc sulphide thin films by chemical bath deposition, J. Alloys Compd. 548 (2013) 166–172.
- [21] J. Madhavi, V. Prasad, ZnS and ZnS/CdS core-shell nano particles: Synthesis, properties and perspectives, Surfaces Interfaces 21 (2020) 100757.
- [22] N. Kaur, S. Kaur, J. Singh, M. Rawat, A review on zinc sulphide nanoparticles: from synthesis, properties to applications, J Bioelectron Nanotechnol 1 (1) (2016) 1–5.
- [23] A. Chakrabarti, E. Alessandri, Syntheses, properties, and applications of ZnS-based nanomaterials, Appl. Nano 5 (3) (2024) 116–142.

- [24] T.-F. Yi, Y. Li, Y.-M. Li, S. Luo, Y.-G. Liu, ZnS nanoparticles as the electrode materials for high-performance supercapacitors, Solid State Ion. 343 (2019) 115074
- [25] S. Saleem, S. Khalid, M.A. Malik, A. Nazir, Review and outlook of zinc sulfide nanostructures for supercapacitors. Energy & Fuels (2024).
- [26] K. Ko, M. Jang, J. Kwon, J. Suh, Native point defects in 2D transition metal dichalcogenides: A perspective bridging intrinsic physical properties and device applications, J. Appl. Phys. 135 (10) (2024).
- [27] I. Hussain, D. Mohapatra, G. Dhakal, C. Lamiel, S.G. Mohamed, M.S. Sayed, J.-J. Shim, Different controlled nanostructures of Mn-doped ZnS for high-performance supercapacitor applications, J. Energy Storage 32 (2020) 101767.
- [28] W. Wang, F. Xiong, S. Zhu, J. Chen, J. Xie, Q. An, Defect engineering in molybdenum-based electrode materials for energy storage, Escience 2 (3) (2022) 278–294.
- [29] A. Rose, B. Shunmugapriya, T. Maiyalagan, T. Vijayakumar, Investigation on the electrochemical properties of hydrothermally synthesized pure and nickel doped zinc sulfide microspheres for supercapacitor electrode applications, J. Mater. Sci., Mater. Electron. 31 (21) (2020) 19204–19212.
- [30] E. Tom, A. Velluva, A. Joseph, T. Thomas, M.S. Sha, P. Jithin, D. Thomas, K.K. Sadasivuni, J. Kurian, Tailoring the electrochemical properties of ZnS electrodes via cobalt doping for improved supercapacitor application, J. Electron. Mater. (2024) 1–11.
- [31] S.G. Mohamed, M.M. Morad, M.R. Siddiqui, A.A. Mahmud, W.A. Zoubi, Improving the electrochemical performance of zinc sulfides by iron doping toward supercapacitor applications, Adv. Mater. Interfaces 11 (4) (2024) 2300790.
- [32] S. Das, A. Banerjee, P. Pal, S. Rudra, U. Nandi, A. Ghosh, Hydrothermally synthesized gadolinium doped molybdenum disulfide for electrochemical supercapacitor applications, J. Energy Storage 99 (2024) 113268.
- [33] A.J. Jebathew, M. Karunakaran, K.D.A. Kumar, S. Valanarasu, V. Ganesh, M. Shkir, I. Yahia, H. Zahran, A. Kathalingam, An effect of Gd³⁺ doping on core properties of ZnS thin films prepared by nebulizer spray pyrolysis (NSP) method, Phys. B 574 (2019) 411674.
- [34] M. Mazhdi, M.J. Tafreshi, The effects of gadolinium doping on the structural, morphological, optical, and photoluminescence properties of zinc oxide nanoparticles prepared by co-precipitation method, Appl. Phys. A 124 (12) (2018) 863
- [35] M. Xin, L.-Z. Hu, Luminescence properties of Zns: Cu, Eu semiconductor nanocrystals synthesized by a hydrothermal process, Chin. Phys. B 22 (8) (2013) 087804.
- [36] M. Xin, L.-M. Liao, F. Han, Optical properties of Zns: Ce nanocrystals prepared by hydrothermal method. J. Lumin. 238 (2021) 118074.
- [37] A.A. Bol, A. Meijerink, Luminescence quantum efficiency of nanocrystalline ZnS: Mn2+. 1. surface passivation and Mn2+ concentration, J. Phys. Chem. B 105 (42) (2001) 10197–10202.
- [38] T. Zahra, B. Alotaibi, A.W. Alrowaily, H.A. Alyousef, A.G. Al-Sehemi, S. Aman, Boosting the energy-storing performance of hydrothermally synthesized ZnO by MnTe for supercapacitor applications, J. Mater. Sci., Mater. Electron. 35 (16) (2024) 1086
- [39] N. Dengo, A. Faresin, T. Carofiglio, M. Maggini, L. Wu, J.P. Hofmann, E.J. Hensen, P. Dolcet, S. Gross, Ligand-free ZnS nanoparticles: as easy and green as it gets, Chem. Commun. 56 (61) (2020) 8707–8710.
- [40] M. Kashif, S. Khan, H. Wajahat, F. Alharbi, A.G. Al-Sehemi, S. Eman, H. Alqurashi, Physicochemical and electrochemical investigation of lead sulphide-graphene oxide hybrid nanostructure for energy storage applications, J. Electroanal. Chem. 974 (2024) 118680.
- [41] A.B. Alwany, G. Youssef, O. Samir, M.A. Algradee, N.A. A. Yahya, M.A. Swillam, S. Humaidi, R. Abd-Shukor, Annealing temperature effects on the size and band gap of ZnS quantum dots fabricated by co-precipitation technique without capping agent, Sci. Rep. 13 (1) (2023) 10314.
- [42] D. Wu, C. Li, D. Zhang, L. Wang, X. Zhang, Z. Shi, Q. Lin, Enhanced photocatalytic activity of Gd³⁺ doped TiO₂ and Gd₂O₃ modified TiO₂ prepared via ball milling method. J. Rare Earths 37 (8) (2019) 845–852.
- [43] R. Dhir, Synthesis, characterization and applications of gadolinium doped ZnS nanoparticles as photocatalysts for the degradation of dyes (Malachite Green and Rhodamine B) and as antioxidants, Chem. Phys. Impact 3 (2021) 100027.
- [44] D. Toloman, M. Stefan, C. Himcinschi, I. Ganea, L. Barbu, A. Rostas, A. Gungor, E. Erdem, A. Popa, Impact of nickel substitution on supercapacitor and photocatalytic performances of cobalt-ferrites nanoparticles, Ceram. Int. (2025).
- [45] D. Toloman, A. Mesaros, A. Popa, T. Silipas, S. Neamtu, G. Katona, V-doped ZnO particles: Synthesis, structural, optical and photocatalytic properties, J. Mater. Sci., Mater. Electron. 27 (2016) 5691–5698.
- [46] W.G. Becker, A.J. Bard, Photoluminescence and photoinduced oxygen adsorption of colloidal zinc sulfide dispersions, J. Phys. Chem. 87 (24) (1983) 4888–4893.
- [47] D. Denzler, M. Olschewski, K. Sattler, Luminescence studies of localized gap states in colloidal ZnS nanocrystals, J. Appl. Phys. 84 (5) (1998) 2841–2845.
- [48] J. Diaz-Reyes, R. Castillo-Ojeda, R. Sánchez-Espíndola, M. Galván-Arellano, O. Zaca-Morán, Structural and optical characterization of wurtzite type Zns, Curr. Appl. Phys. 15 (2) (2015) 103–109.
- [49] Y.-T. Nien, I.-G. Chen, Raman scattering and electroluminescence of Zns: Cu, Cl phosphor powder, Appl. Phys. Lett. 89 (26) (2006).

I. Nesterovschi et al.

- [50] C. Bi, L. Pan, M. Xu, J. Yin, Z. Guo, L. Qin, H. Zhu, J.Q. Xiao, Raman spectroscopy of co-doped wurtzite ZnS nanocrystals, Chem. Phys. Lett. 481 (4–6) (2009) 220–223.
- [51] M. Dimitrievska, H. Xie, A. Jackson, X. Fontané, M. Espíndola-Rodríguez, E. Saucedo, A. Pérez-Rodríguez, A. Walsh, V. Izquierdo-Roca, Resonant raman scattering of ZnS_xSe_{1-x} solid solutions: the role of s and se electronic states, Phys. Chem. Chem. Phys. 18 (11) (2016) 7632–7640.
- [52] U. Gawai, U. Deshpande, B. Dole, A study on the synthesis, longitudinal optical phonon-plasmon coupling and electronic structure of al doped ZnS nanorods, RSC Adv. 7 (20) (2017) 12382–12390.
- [53] Y. Cheng, C. Jin, F. Gao, X. Wu, W. Zhong, S. Li, P.K. Chu, Raman scattering study of zinc blende and wurtzite ZnS, J. Appl. Phys. 106 (12) (2009).
- [54] S. Radhu, C. Vijayan, Observation of red emission in wurtzite ZnS nanoparticles and the investigation of phonon modes by Raman spectroscopy, Mater. Chem. Phys. 129 (3) (2011) 1132–1137.
- [55] Y. Shono, T. Oka, Complex defects in electron-irradiated ZnS, J. Cryst. Growth 210 (1–3) (2000) 278–282.
- [56] J. Schneider, A. Räuber, Electron spin resonance of the F-centre in ZnS, Solid State Commun. 5 (9) (1967) 779–781.
- [57] Y. Vaills, J. Buzare, Epr studies of ${\rm Gd^{3+}}$ centres in the cubic phase of ${\rm CsCaCl_3}$ and ${\rm CsPbCl_3}$, J. Phys. Chem. Solids 48 (4) (1987) 363–370.
- [58] S. Smith, T. Cole, Noncubic epr spectra of Gd³⁺ in CdF₂, J. Chem. Phys. 52 (3) (1970) 1286–1292.
- [59] N. Kozhevnikova, M. Melkozerova, A. Enyashin, A. Tyutyunnik, L. Pasechnik, I. Baklanova, A.Y. Suntsov, A. Yushkov, L.Y. Buldakova, M.Y. Yanchenko, Janus ZnS nanoparticles: Synthesis and photocatalytic properties, J. Phys. Chem. Solids 161 (2022) 110459.
- [60] M. Ali, S. Gouadria, F. Alharbi, M. Abdullah, S. Aman, H.M.T. Farid, Development of Ce-doped SrTiO3 low-cost electrode material for supercapacitor applications, J. Mater. Sci., Mater. Electron. 36 (5) (2025) 1–14.
- [61] A.W. Alrowaily, M. Abdullah, B. Alotaibi, H.A. Alyousef, M.F. Alotiby, S. Aman, A.G. Al-Sehemi, A. Henaish, Hydrothermally synthesized neodymium-doped Co3O4 nanostructures as electrode for supercapacitor applications, J. Mater. Sci., Mater. Electron. 36 (4) (2025) 246.
- [62] A.M. Rostas, A. Gungor, A.M. Kasza, F.B. Misirlioglu, A. Turza, L. Barbu-Tudoran, E. Erdem, M. Mihet, Zinc oxide-decorated MIL-53 (al)-derived porous carbon for supercapacitor devices, J. Mater. Chem. C 13 (20) (2025) 10342–10355.
- [63] W.K. Chee, H.N. Lim, I. Harrison, K.F. Chong, Z. Zainal, C.H. Ng, N.M. Huang, Performance of flexible and binderless polypyrrole/graphene oxide/zinc oxide supercapacitor electrode in a symmetrical two-electrode configuration, Electrochim. Acta 157 (2015) 88–94.
- [64] J.P.A. dos Santos, F.C. Rufino, J.I.Y. Ota, R.C. Fernandes, R. Vicentini, C.J. Pagan, L.M. Da Silva, H. Zanin, Best practices for electrochemical characterization of supercapacitors, J. Energy Chem. 80 (2023) 265–283.

- [65] R. Raavi, S. Archana, P.A. Reddy, P. Elumalai, Performances of dual carbon multi-ion supercapacitors in aqueous and non-aqueous electrolytes, Energy Adv. 2 (3) (2023) 385–397.
- [66] M.Z. Iqbal, M.M. Faisal, M. Sulman, S.R. Ali, A.M. Afzal, M.A. Kamran, T. Alharbi, Capacitive and diffusive contribution in strontium phosphide-polyaniline based supercapattery, J. Energy Storage 29 (2020) 101324.
- [67] M. Hussain, L.A. El Maati, M.A. Alomar, M. Ali, M. Abdullah, S. Aman, H.M.T. Farid, Enhancement of capacitive properties of Ce-doped MnAl2O4 electrode for high performance energy storage applications, Jom 76 (8) (2024) 4587–4597.
- [68] L.A. El Maati, R.Y. Khosa, S.D. Alahmari, F. Alharbi, M. Abdullah, S. Aman, A.G. Al-Sehemi, A. Henaish, Z. Ahmad, H.M.T. Farid, Facile synthesis of environmental friendly Sm2O3/rGO electrode as an alternative source for energy storage devices, Diam. Relat. Mater. 142 (2024) 110769.
- [69] A.C. Lazanas, M.I. Prodromidis, Electrochemical impedance spectroscopy a tutorial, ACS Meas. Sci. Au 3 (3) (2023) 162–193.
- [70] A. Ali, M. Aadil, A. Rasheed, I. Hameed, S. Ajmal, I. Shakir, M.F. Warsi, Honeycomb like architectures of the Mo doped ZnS@ Ni for high-performance asymmetric supercapacitors applications, Synth. Met. 265 (2020) 116408.
- [71] G.S. Kaliaraj, A. Ramadoss, Nickel-zinc sulfide nanocomposite thin film as an efficient cathode material for high-performance hybrid supercapacitors, Mater. Sci. Semicond. Process. 105 (2020) 104709.
- [72] N. Abbas, I. Shaheen, I. Hussain, C. Lamiel, M. Ahmad, X. Ma, A. Qureshi, J.H. Niazi, M. Imran, M.Z. Ansari, et al., Glycerol-mediated synthesis of copper-doped zinc sulfide with ultrathin nanoflakes for flexible energy electrode materials, J. Alloys Compd. 919 (2022) 165701.
- [73] X. Hou, T. Peng, J. Cheng, Q. Yu, R. Luo, Y. Lu, X. Liu, J.-K. Kim, J. He, Y. Luo, Ultrathin ZnS nanosheet/carbon nanotube hybrid electrode for high-performance flexible all-solid-state supercapacitor, Nano Res. 10 (2017) 2570–2583.
- [74] M. Hussain, B. Alotaibi, A.W. Alrowaily, H.A. Alyousef, M.F. Alotiby, M. Abdullah, A.G. Al-Sehemi, A. Henaish, Z. Ahmad, S. Aman, Synthesis of high-performance supercapacitor electrode materials by hydrothermal route based on ZnSe/MnSe composite, J. Phys. Chem. Solids 188 (2024) 111919.
- [75] M. Zeshan, S. Eman, A.M. Fallatah, M.M. Ibrahim, A.S. Almalki, M. Aslam, Z.M. El-Bahy, Facile fabrication of binary metal chalcogenides (MS@ NS) for supercapacitors applications via hydrothermal route, J. Sol-Gel Sci. Technol. 113 (3) (2025) 855–867.
- [76] G. Nabi, W. Raza, M.A. Kamran, T. Alharbi, M. Rafique, M.B. Tahir, S. Hussain, N. Khalid, N. Malik, R.S. Ahmed, et al., Role of cerium-doping in CoFe2O4 electrodes for high performance supercapacitors, J. Energy Storage 29 (2020) 101452.
- [77] L. Yang, Z. Zhang, J. Liu, L. Huang, L. Jia, Y. Feng, Influence of gd doping on the structure and electrocatalytic performance of TiO2 nanotube/SnO2- Sb nano-coated electrode, ChemElectroChem 5 (22) (2018) 3451–3459.